Read and write amplitude and phase information by using high-precision molecular wave-packet interferometry

Hiroyuki Katsuki,[1,2,3] Kouichi Hosaka,[1,3] Hisashi Chiba,[1,3] and Kenji Ohmori[1,2,3,*]
[1]*Institute for Molecular Science, National Institutes of Natural Sciences, Okazaki 444-8585, Japan*
[2]*SOKENDAI (The Graduate University for Advanced Studies), Okazaki 444-8585, Japan*
[3]*CREST, Japan Science and Technology Agency, Kawaguchi, Saitama 332-0012, Japan*
(Received 5 February 2007; published 11 July 2007)

We demonstrate an experimental approach to read and write populations and relative phases of vibrational eigenstates within a wave packet created in the B state of the iodine molecule by using a pair of phase-locked femtosecond laser pulses. Our highly stabilized optical interferometer provides attosecond stability and resolution in the interpulse delay. The stability and resolution have realized an exquisite tuning of the interference of two vibrational wave packets to manipulate the relative populations and the relative quantum phases among the vibrational eigenstates within the wave packets. These populations and phases have been retrieved by measuring fluorescence from the upper E state induced by another nanosecond (ns) or femtosecond (fs) probe laser pulse. The bandwidth of the ns probe pulse is narrow enough to select only a small portion of the rotational progression of a particular vibrational band of the $E-B$ transition. By scanning the probe wavelength, we measure the population distribution of the vibrational eigenstates within the wave packet. The fs probe pulse is used to measure quantum beats arising from the temporal evolution of the wave packet. Combining these two complementary measurements, we can read both population and phase information written and stored in the wave packet.

DOI: 10.1103/PhysRevA.76.013403 PACS number(s): 42.50.Md, 33.80.−b, 39.30.+w, 82.53.Kp

I. INTRODUCTION

Wave-packet interferometry (WPI) is a clear manifestation of the wave nature of quantum objects. It is based on a technique to control the relative phase of two WPs created in an atom or a molecule. One of the most straightforward methods to create such a phased pair of WPs is to use a pair of femtosecond (fs) laser pulses whose relative phase is locked. Scherer *et al.* applied this technique to the iodine molecule and controlled an interference of two vibrational WPs created on the B state potential curve. They measured fluorescence from the B state [1,2] as a function of the relative phase of the twin fs laser pulses, and observed that the fluorescence intensity was clearly sensitive to the relative phase.

After their pioneering works, the phase-locked double pulse approach has so far been developed with Rydberg and spin-orbit WPs in atoms and molecules [3–16] and vibrational and rotational WPs in molecules [1,2,17–23] based on the measurement of population of the bound excited state sensitive to the relative phase of the twin optical pulses. Aside from such bound-state interferometry, WP interference has also been observed for the free states located above the dissociation limits of the relevant potential curves [24–28]. Similar double pulse approaches have also been applied to condensed phases [29,30].

In our previous papers [20,21], we demonstrated our high-precision bound-state WPI with the HgAr van der Waals complexes and the iodine molecules. The thermal distribution of rotational states is known to be a major source of decoherence in molecular systems that can wipe out the interference structure much more quickly than in atomic systems [1,2,17–19]. We succeeded in drastically reducing this rotational dephasing by employing a cold and dilute ensemble of the molecules prepared by the supersonic jet expansion and narrow-band interrogation of the state populations with a nanosecond (ns) probe laser pulse. The high-precision WPI was then employed to manipulate the population distribution of the vibrational eigenstates within WPs, and that population information was retrieved by state-selective interrogation [20,21]. The state-selective population measurements were further combined with the real-time observation of the WP interference to retrieve both amplitude and phase information stored in WPs [21]. The experiments for this combined approach were, however, carried out with the ensemble of the different initial vibrational levels; $v_X \sim 1-4$ of the ground electronic state of the iodine molecules. This is because of our choice of the excitation wavelengths for which the Franck-Condon factors are quite unbalanced among different v_X's, much more favorable for the higher v_X's.

In this paper, we report the details of our high-precision molecular WPI, and its application to the amplitude- and phase-information processing with the iodine molecules under clearer conditions. In the present choice of the excitation wavelength, the contribution of the initial vibrational level $v_X=0$ is predominant. Therefore it becomes easier to make detailed comparisons between experimental results and theoretical calculations. We will demonstrate how to read and write with molecular vibrational WPs by using tightly phase-locked double pulse combined with amplitude- and phase-sensitive detections with another probe pulse. We use a narrow-band ns probe laser pulse for the amplitude-sensitive detection. The bandwidth of this ns pulse is narrow enough to selectively probe one particular vibrational eigenstate

*Electronic address: ohmori@ims.ac.jp

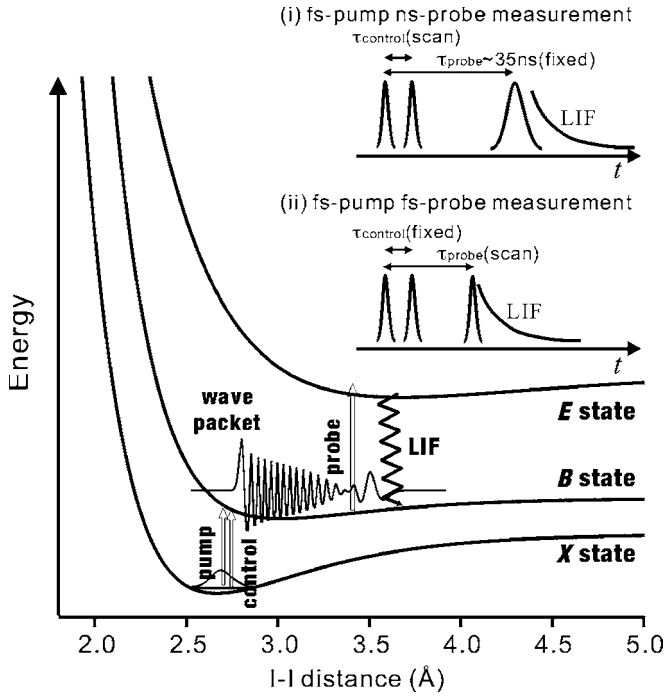

FIG. 1. Pump-control-probe scheme for the real-time or state-resolved measurement of wave-packet interference with the fs or ns probe pulse. The potentials are only schematic.

within a WP. By scanning its wavelength, therefore, the populations of the vibrational eigenstates within the WP are measured. We have another choice to use a broadband fs probe pulse for the phase-sensitive detection. By using this fs probe pulse, we can track the temporal evolution from the generation of the first WP to its interference with the second WP, which is highly sensitive to the relative phases among the vibrational eigenstates within the WP. Combining these two complementary detection schemes, we could obtain both the amplitude and phase information written and stored in the WP.

This paper is organized as follows. In Sec. II, our experimental system is described. Theoretical background of the phase-locked double-pulse excitation is presented in Sec. III. The experimental results are presented in Sec. IV. Comparisons of the experimental results and theoretical simulations are discussed in Sec. V. In Sec. VI, our approach is compared with other approaches reported so far. Finally, concluding remarks are given in Sec. VII.

II. EXPERIMENT

Figure 1 depicts the scheme of our experiment. Two vibrational WPs were created in the B electronic state of the I_2 molecule by using a phase-locked pair of pump and control pulses with their relative delay τ_{control}. The relative position and phase of those two WPs can be arbitrarily controlled by tuning τ_{control}. The WPs created by the pump and control pulses interact with each other and create complicated interference structures. Another laser pulse (fs or ns) served as a probe pulse with its delay τ_{probe}. This probe pulse brings the portion of the WP amplitude in the B state to the upper E state, from which we measure fluorescence with a photomultiplier via a monochromator.

Similar experiments without the control pulse were done in the same iodine system by Gruebele *et al.* in the beginning of 1990's [31,32]. They obtained the molecular constants and the relevant potential curves from the temporal evolution of a single WP. Using the phase-locked control pulse, we have incorporated one more free parameter, τ_{control}, which enables us to actively control the structure of the WP.

The experimental apparatus was similar to the one used in our previous paper on the HgAr van der Waals complexes [20], but was newly constructed for the present studies [21]. A Ti:Sapphire mode locked laser and a regenerative amplifier (Quantronix, Titan) were used to prepare ~100 fs pulses around 800 nm at a 1 kHz repetition rate instead of the previous 10 Hz system. These pulses were converted to around 530 nm with an optical parametric amplifier (OPA) (Quantronix, TOPAS), which was newly incorporated, and were used for the pump and control pulses. The bandwidth of this 530 nm pulse was ~4 nm in full width at half maximum (FWHM). This bandwidth was reduced in the present experiments to cover only four vibrational levels $v_B=30-33$ in the B state; we stretched the pulse with a grating and discarded its high- and low-frequency tails with thin metal blades. And only the central frequency part (5.7 nm from edge to edge) which covers $v_B=30-33$ was recompressed. Because of this reduction in the bandwidth, the temporal FWHM of the pump and control pulses was elongated.

The recompressed pulse was input to a homemade Michelson interferometer [20,21], which we call an attosecond phase modulator (APM). The phase-locked pump and control pulses were generated with this APM. The optical paths within APM were highly stabilized by assembling all optical components in a vacuum chamber. The relative delay (τ_{control}) was coarsely tuned by sliding a mechanical translation stage inserted in one arm of APM; while its fine tuning was done by changing the gas pressure within a stainless cell (~15 cm in length and ~20 mm in inner diameter) installed in the other arm of APM. Argon was used in this pressure tuning of τ_{control} in the present study. The spectrum of the double pulse produced by APM was monitored with a 50 cm spectrometer (Nikon G-500) equipped with a grating (1200 lines/mm) and coupled with a 1024-channel linear detector (Hamamatsu S3904-1024Q), whose outputs were fed into a personal computer. We have introduced a feedback-loop control of the mechanical stage, which was specially designed to reduce its heat-induced deformation (Suruga Seiki TKS102-30). These features have improved the long-time stability and the resolution of τ_{control} in comparison with our previous system [20]. For the measurements made with τ_{control} fixed to a specific value, the feedback control of τ_{control} was carried out in every ~6 seconds to compensate the deviation of the double-pulse spectrum monitored in real time by the linear detector with a tolerance of ±20 attoseconds, which corresponds to $\pm 0.023\pi$ in the relative phase $\theta_{\text{p-c}}$ of the pump and control pulses and is regarded as a typical upper limit of the long-time stability. The energies of the pump and control pulses were ~10 μJ.

We employed two different types of interrogation as shown in the small insets of Fig. 1 [21] to obtain both the

amplitude and phase information of the WP. In scheme (i), we used a ns probe pulse which was generated by a dye laser (Lambda Physik, SCANmate 2E, dye:Exciton, Exalite 398) pumped by a XeCl excimer laser (Lambda Physik, COMPex 110). We obtained 30 μJ/pulse at a 50 Hz repetition rate. The ns probe pulse was delayed from the pump pulse by ~35 ns with ±5 ns jitter, and its bandwidth was about 0.03 cm^{-1}. This bandwidth allowed us to select a small portion of the rotational progression within a specific vibrational band of the $E \leftarrow B$ transition. By scanning the ns probe wavelength from ~400 to 402 nm, we obtain the excitation spectrum, which we call a "population code." The population code retrieves the population information of the vibrational eigenstates within the WP. Since the typical life time of the vibrational levels of the B state is on the order of 1.1 μs [33,34] and is much longer than the probe delay, the population code is the population distribution of the vibrational eigenstates prepared by the pump and control pulses weighted with their corresponding Franck-Condon factors (FCFs) of the relevant $E \leftarrow B$ transitions. In scheme (ii), the ns probe pulse was replaced by a fs probe pulse to measure quantum beats arising from the WP motion on the B state potential; the fs probe pulse was prepared by another OPA (Quantronix, TOPAS) and was centered around 429 nm. Its bandwidth was ~5 nm. By tuning τ_{control} on the attosecond time scale, we can control the interference of two WPs, so that the shape and phase of the beat structure change drastically. Careful analyses of this beat structure, which we call a "phase code," retrieve information on the relative phases of the vibrational eigenstates within the WP. In the following sections, we will show how precisely this population and phase codes can be controlled with our pump and control pulses tightly phase locked on the attosecond time scale.

In another type of measurements made with the ns probe pulse, we fixed the wavelength of the ns probe pulse to around the top of a particular vibrational band of the $E \leftarrow B$ transition and scanned τ_{control} by increasing the pressure of the gas cell within the APM. This measurement yielded an interferogram of a particular vibrational eigenstate within the WP, which we call an "eigenstate interferogram" in the present paper. By switching the ns probe wavelength from one vibrational band to another vibrational band with the gas-pressure scanned at a constant speed, the relative phase between those two different eigenstate interferograms can be obtained. Similar measurements have been done previously for the HgAr van der Waals complexes [20]. We call this measurement a "phase-jump measurement" in the present paper. This phase jump measurement is necessary to tune the timing τ_{control} of the pump and control pulses to manipulate the population code and the phase code.

The cold I_2 molecules were prepared in the electronic ground state ($X^1\Sigma_g^+$) by an expansion of heated I_2/Ar mixture (~330 K, ~2 atm) into a vacuum chamber through a pulsed nozzle (Parker Hannifin, General Valve model 009-0506-900) driven at a repetition rate of 50 Hz. With this repetition rate we lost 95% of the pump and control pulses, but the pulsed nozzle assured higher signal intensities and lower rotational temperatures than those obtained with the continuous jet expansion used in our previous paper [21]. The vibrational and rotational temperatures of our ensemble of I_2 were estimated from the $B-X$ fluorescence excitation spectra measured by scanning the wavelength of the narrow-band dye laser around 573–575 nm. These excitation spectra were taken without shining the pump and control pulses. The vibrational temperature was estimated to be ~200 K, under which the population of $v_X=1$ is about 20% of that of $v_X=0$, and the rotational temperature was estimated to be around 2 K. In the 530 nm region covered by the pump and control pulses, FCFs of the $B-X$ transitions from $v_X=0$ are at least five times larger than those of the transitions from $v_X=1$ [35]. Therefore, the contributions of the hot bands to the B-state populations are estimated to be less than 4%. In the following analysis, we consider the transitions only from $v_X=0$.

III. THEORETICAL BACKGROUND

In the following discussion, we do not take into account the rotational degree of freedom for simplicity. The influence of the rotational distribution could be seen, if any, in the slow modulation (on the picosecond time scale) of the beat measured with the fs probe pulse, and/or the shaded spectral shape of each vibrational band measured with the ns probe pulse. Furthermore, the interaction of the WP with the probe pulse is omitted since we concentrate on the structure of the WP created by the pump and control pulses. The system Hamiltonian has the form

$$H = |X\rangle H_X \langle X| + |B\rangle (H_B + \hbar\omega_{BX}) \langle B| + V(t), \tag{1}$$

where $|X\rangle$ and $|B\rangle$ denote the electronic ground state and the electronic excited state ($B^3\Pi_{0_u^+}$), respectively. H_X and H_B are the vibrational Hamiltonians of the X and the B electronic states, and ω_{BX} denotes the 0-0 vibronic transition frequency. The interaction part corresponding to the $B \leftarrow X$ transition is written as

$$V(t) = |B\rangle V_1(t) \langle X| + \text{c.c.}, \tag{2}$$

$$V_1(t) = -\mu_{BX} E_{pc}(t), \tag{3}$$

where μ_{BX} is the dipole moment operator connecting the two relevant electronic states. The electric field E_{pc} of the pump and control pulses generated from APM is given by

$$E_{pc}(t, \tau_{\text{control}}) = E_0(t)\cos(\omega_0 t) + E_0(t - \tau_{\text{control}})\cos(\omega_0 (t - \tau_{\text{control}})), \tag{4}$$

where the intensity difference between the pump and control pulses is considered negligible, and ω_0 denotes their carrier angular frequency. For simplicity, we assume the Gaussian profile for $E_0(t)$ as

$$E_0(t) = E_0 \exp\left[-\left(\frac{t}{\tau_G}\right)^2\right]. \tag{5}$$

The modulus square of the Fourier transform of the above electric field gives the spectrum of the double pulse:

$$|E_{pc}(\omega)|^2 \cong 2E_0^2\tau_G^2\pi \exp\left(-\frac{(\omega-\omega_0)^2\tau_G^2}{2}\right)[1+\cos(\omega\tau_{\text{control}})], \tag{6}$$

where we keep only the slowly varying envelope components. From Eq. (6) it is seen that the intensity of each frequency component oscillates with a frequency ω as τ_{control} is scanned. We consider only the linear interaction with $V(t)$. The B-state wave function after the interaction with the pump and control pulses is

$$|\Psi_B(t)\rangle = -i\hbar\int_0^t e^{-iH_B(t-t')/\hbar}V_1(t')e^{-iH_X t'/\hbar}|\Psi_0\rangle dt', \tag{7}$$

where $|\Psi_0\rangle$ is the initial-state vibronic wave function. As explained in the last section, we consider only $v_X=0$ as $|\Psi_0\rangle$. It is seen from Eqs. (3), (4), and (7) that $|\Psi_B(t)\rangle$ is composed of two terms representing the two WPs created by the pump and control pulses, respectively.

Population ρ_n of a particular vibrational level $v_B=n$ within the B-state WP created by a sequence of the pump and control pulses is given by

$$\begin{aligned}\rho_n &= |\langle v_B=n,B|\Psi_B(t)\rangle|^2 = \hbar^2|\mu_{n0}|^2\left|\int_0^t E_{pc}(t',\tau_{\text{control}})e^{i\omega_n t'}dt'\right|^2 \\ &= \hbar^2|\mu_{n0}|^2|E(\omega_n)|^2 = 2\hbar^2|\mu_{n0}|^2E_0^2\tau_G^2\pi\exp\left(-\frac{(\omega_n-\omega_0)^2\tau_G^2}{2}\right) \\ &\quad\times[1+\cos(\omega_n\tau_{\text{control}})],\end{aligned} \tag{8}$$

where ω_n is the transition frequency of $v_B=n$ for the transition from the initial vibrational level $v_X=0$, and μ_{n0} is the matrix element of the transition dipole moment between these two vibrational states. As we scan τ_{control}, therefore, the population of $v_B=n$ oscillates with the frequency ω_n. This eigenstate interferogram can be directly measured in the interrogation scheme (i) where we use the ns probe pulse to detect the laser-induced fluorescence signal originating from one particular vibrational level within the B-state WP. Note that the last term of Eq. (8) is not characteristic to the Gaussian profile of $E_0(t)$ assumed here, but is common to any profiles of $E_0(t)$.

Before considering the interference of the two WPs created by the pump and control pulses, we briefly discuss the temporal evolution of a single WP created by the pump pulse alone. A vibrational WP is created by the pump pulse around the inner classical turning point of the B-state potential curve. Following the theoretical approach by Averbukh and Perelman [36], the frequency ω_n is expanded around the frequency $\omega_{\tilde{n}}$ of the level $v_B=\tilde{n}$:

$$\omega_n = \omega_{\tilde{n}} + (n-\tilde{n})\left.\frac{d\omega_n}{dn}\right|_{n=\tilde{n}} + \frac{1}{2}(n-\tilde{n})^2\left.\frac{d^2\omega_n}{dn^2}\right|_{n=\tilde{n}} + \cdots, \tag{9}$$

where $\tilde{n}$ is an integer, and $\omega_{\tilde{n}}$ is close to the carrier frequency of the pump pulse. The classical vibrational period, T_{vib}, is then defined as

$$T_{\text{vib}} = \frac{2\pi}{\left.\frac{d\omega_n}{dn}\right|_{n=\tilde{n}}}. \tag{10}$$

If the second- and higher-order terms in Eq. (9) are neglected, that is, if the potential is harmonic, T_{vib} is the timing when the phase difference between the adjacent vibrational levels $v_B=n$ and $n+1$ is 2π. Therefore, the WP regains its original position and shape with a period of T_{vib}. In the realistic situation, however, the second-order term in Eq. (9) is not zero, and anharmonicity of the potential curve needs to be considered. Hence the relative phases among the vibrational levels within the WP are not completely recovered with a period of T_{vib}, but the WP gradually collapses. The revival time, T_{rev}, is then defined for such realistic situations as

$$T_{\text{rev}} = \frac{4\pi}{\left|\left.\frac{d^2\omega_n}{dn^2}\right|_{n=\tilde{n}}\right|}. \tag{11}$$

In the temporal regions around $1/2T_{\text{rev}}$ and T_{rev}, the phase factor arising from the second-order term of Eq. (9) is close to $(n-\tilde{n})^2\pi$ and $2(n-\tilde{n})^2\pi$, respectively. Accordingly, the WP regains its almost original position and shape with a period of T_{vib} in these temporal regions. This is the origin of the well-known half and full revivals of WPs [37–41].

Under the present experimental conditions, the level $v_B=32$ is taken to be a reference state so that $\tilde{n}=32$, and then $\left.\frac{d\omega_n}{dn}\right|_{n=32}$ and $\left.\frac{d^2\omega_n}{dn^2}\right|_{n=32}$ are evaluated to be 66 cm^{-1} and -2.1 cm^{-1}, respectively. Furthermore, only four vibrational levels $v_B=30-33$ are covered by the pump pulse, so that the ratio of the coefficients of the second-order term to the first-order term in Eq. (9) is no more than 1. Accordingly, the first-order term in Eq. (9) is larger than the second-order term by a factor of more than 30 for any possible n. The periods T_{vib} and T_{rev} are then evaluated to be 505.4 fs and 31.8 ps, respectively. Since T_{vib} is much shorter than T_{rev}, and the second-order term is much smaller than the first-order term for any n, we expect to see many recurrences of the WP with a period of T_{vib} before it collapses.

IV. RESULTS AND DISCUSSION

A. Performance of APM

We have measured an optical interferogram of the pump and control pulses whose carrier wavelengths were tuned to ~537 nm. The purpose of this measurement was to evaluate the performance of our APM. In this measurement, τ_{control} was coarsely tuned to ~0 fs with the mechanical stage so that the pump and control pulses were temporally superimposed. The total laser intensity was measured by a Si diode detector while the argon pressure within the gas cell was scanned. The measured interferogram is plotted linearly against the number of data points N in Fig. 2 together with a sine curve least square fitted to the measured interferogram. Since the data acquisition cycle was kept constant during the measurement, the number N is linear to the pressure scan-

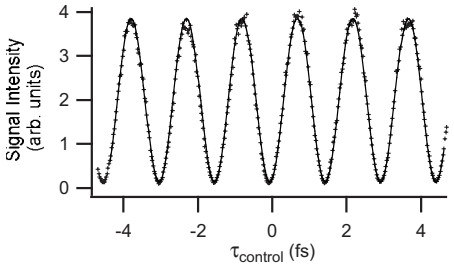

FIG. 2. Example of the optical interferogram measured around $\tau_{\text{control}} \sim 0$ fs. One cycle of the oscillation corresponds to 1.79 fs. The solid curve represents a sine curve least square fitted to the measured interferogram. One standard deviation of the oscillation period is 700 zeptoseconds.

ning time. The abscissa is the delay τ_{control} which was calibrated by an optical cycle 1.79 fs of the present carrier wavelength 537 nm; the period N_{fit} (in the number of data points) of the fitted sine curve corresponds to 1.79 fs. The origin of the delay, $\tau_{\text{control}}=0$, is arbitrary. The variation of τ_{control} is linearly dependent on the variation of the argon pressure; ~6 Torr corresponds to 1 fs under the present experimental conditions. In every interferogram measured in the present study, however, the delay τ_{control} was calibrated by the period of the measured interferogram itself to avoid any possible errors arising from uncertainties in measuring the actual argon pressure averaged along the optical path within the cell.

In scanning the argon pressure within the cell, the argon gas was introduced into the cell from a high-pressure argon reservoir through a high-precision needle valve (GRANVILLE-PHILLIPS, Variable Leak 203). Since the pressure of the reservoir was kept constant around 1.1 atm, the rate of the pressure-increase within the cell gradually becomes lower, so that the period of the interferogram gradually becomes longer. This effect may not be negligible for a long pressure scan. In every interferogram displayed and analyzed in the present paper, however, we have used no more than six successive periods of the interferogram. We have compared the periods N_{fit}'s of sine curves fitted, respectively, to the first and second half of the successive six periods of the optical interferogram shown in Fig. 2, and their difference has been verified to be less than 1%. Therefore, we neglect the effect of nonlinearity in the abscissas of the interferograms shown in the present paper, and all the interferograms are plotted linearly against the number of data points N, which is linear to the pressure scanning time. One standard deviation of the oscillation period of the fitted sine function shown in Fig. 2 is 700 zeptoseconds.

B. Eigenstate interferogram

Figure 3 shows a set of the phase-jump measurements made by scanning τ_{control} around 500 fs ($\cong 1T_{\text{vib}}$), where T_{vib} is a classical vibrational period of I_2. In the actual measurement, T_{vib} is determined from the period of the sine curve fitted to the beat structure measured without the control pulse.

This pump-control timing gives the situation where the second WP is created when the first WP comes back to the

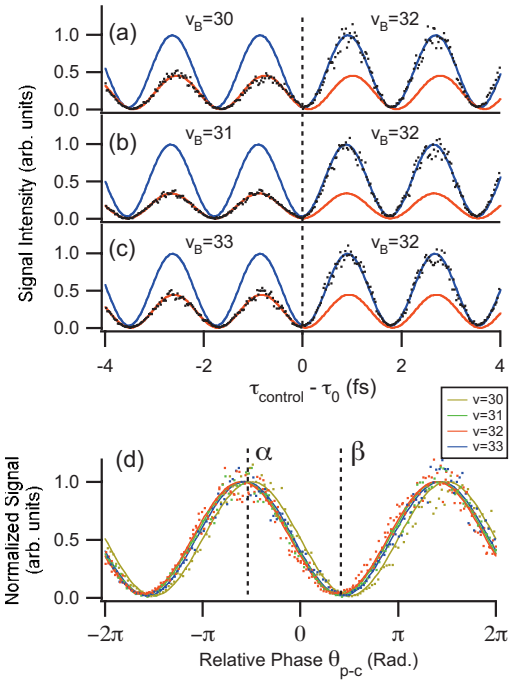

FIG. 3. (Color) Interferogram of each vibrational eigenstate within the wave packets, which we call an "eigenstate interferogram," measured with the pump-control delay τ_{control} tuned around $1T_{\text{vib}}$, where T_{vib} is a classical vibrational period of I_2. In the upper three panels (a), (b), and (c), the probe wavelength was switched from one vibrational band to another vibrational band at $\tau_{\text{control}} - \tau_0 \simeq 0$ as τ_{control} was scanned toward a negative direction: (a) $v_E = 25 \leftarrow v_B = 32$ (right) to $24 \leftarrow 30$ (left), (b) $25 \leftarrow 32$ (right) to $25 \leftarrow 31$ (left), and (c) $25 \leftarrow 32$ (right) to $26 \leftarrow 33$ (left). The abscissas of (a), (b), and (c) were calibrated by the periods of the interferograms calculated from the relevant spectroscopic constants [42]. Black curves are measured data, and blue and red curves are the sine functions least square fitted to the regions on the right and left sides of the switching point, $\tau_{\text{control}} - \tau_0 = 0$, respectively. In the lowest panel, the four different eigenstate interferograms are plotted together with their relative phases determined in the upper three panels. See text for further details.

initial Franck-Condon region, which is located around the inner turning point of the B-state potential curve; the two WPs are spatially superimposed with each other. We experimentally verified that the optical interference of the pump and control pulses was negligible with this τ_{control}.

The delay τ_{control} was scanned toward a negative direction in the present measurements by increasing the pressure of the gas cell of APM. In each of the upper three panels of Fig. 3, we started recording an interferogram with the probe wavelength tuned to the vibrational band $v_E = 25 \leftarrow v_B = 32$. After scanning for about three periods, the probe wavelength was switched to the different vibrational band: $v_E = 24 \leftarrow v_B = 30$, $25 \leftarrow 31$, or $26 \leftarrow 33$. It is seen that the relative phase of two different eigenstate interferograms are clearly visualized in these phase-jump measurements. The abscissa represents the relative value of the pump-control delay $\tau_{\text{control}} - \tau_0$, where τ_0 is the timing when the probe wavelength was switched in each scan. Black dots are measured data, and blue and red curves are the sine functions least square fitted to the regions

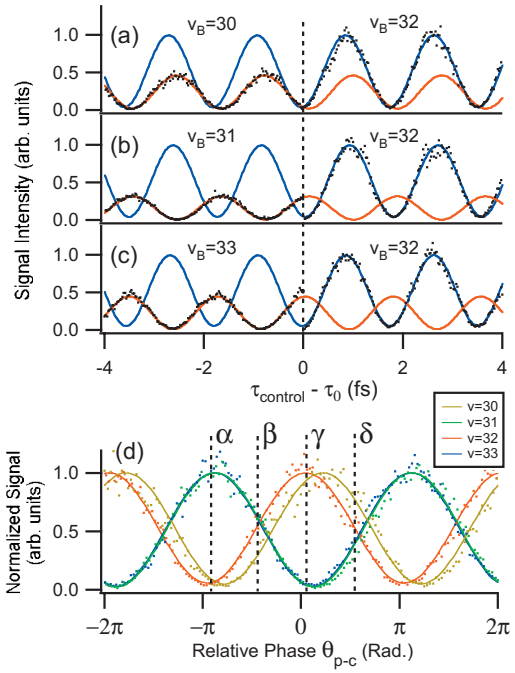

FIG. 4. (Color) Eigenstate interferogram measured with the pump-control delay $\tau_{control}$ tuned around $(1+1/2)\ T_{vib}$, where T_{vib} is a classical vibrational period of I_2. For the explanation of (a), (b), and (c), see the caption of Fig. 3. Black curves are measured data, and blue and red curves are the sine functions least square fitted to the regions on the right and left sides of the switching point, $\tau_{control}-\tau_0=0$, respectively. In the lowest panel, the four different eigenstate-interferograms are plotted together with their relative phases determined in the upper three panels. See text for further details.

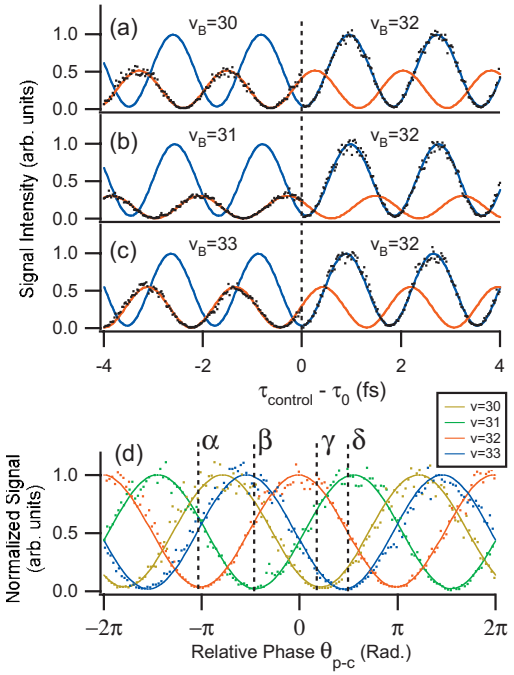

FIG. 5. (Color) Eigenstate interferogram measured with the pump-control delay $\tau_{control}$ tuned around $(1+1/4)\ T_{vib}$, where T_{vib} is a classical vibrational period of I_2. For the explanation of (a), (b), and (c), see the caption of Fig. 3. Black curves are measured data, and blue and red curves are the sine functions least square fitted to the regions on the right and left sides of the switching point, $\tau_{control}-\tau_0=0$, respectively. In the lowest panel, the four different eigenstate interferograms are plotted together with their relative phases determined in the upper three panels. See text for further details.

on the right and left sides of the switching point, $\tau_{control}-\tau_0=0$, respectively. As is clearly seen from Eq. (8), each eigenstate interferogram of the level $v_B=n$ shown in Fig. 3 oscillates with a period of $T_{spec}=2\pi/\omega_n$, where ω_n is the transition frequency of $v_B=n$ for the transition from $v_X=0$. In each of the three phase-jump measurements shown in the upper panels of Fig. 3, therefore, the periods T_{spec}'s of the interferograms on the right and left sides of the switching point differ by less than 0.8%, which was derived with the values of ω_n's taken from a previous spectroscopic study [42]. Since the difference is thus negligible, the periods of the two fitted sine functions shown in each panel were fixed to an average N_{ave} of the periods N_{fit}'s of two sine functions fitted independently to the regions on the right and left sides of the switching point, respectively, in the present analysis. The abscissa was then calibrated in each panel so that N_{ave} corresponded to the average of those two T_{spec}'s. These fitting and calibration procedures are common to all of the eigenstate interferograms shown in Figs. 3–6.

In the lowest panel, the four different eigenstate interferograms are normalized and plotted together with their relative phases determined in the upper three panels. In this plot, the measured interferograms of $v_B=30$, 31, and 33 are shifted horizontally by two or three oscillation cycles of their own fitted sine functions to be superposed on the reference interferograms of $v_B=32$. The relative delay $\tau_{control}-\tau_0$ of the pump and control pulses is now converted to their relative phase θ_{p-c} of the pump and control pulses.

Another set of the phase-jump measurements has been made by scanning $\tau_{control}$ around 760 fs $[\cong(1+1/2)T_{vib}]$, and its results are shown in Fig. 4. With this pump-control timing, the second WP is created around the inner turning point of the potential curve when the first WP is traveling around the outer turning point. Again the relative phase of two different eigenstate interferograms is clearly visualized in each of the upper three panels of Fig. 4. By comparing Figs. 3(a)–3(c) and Figs. 4(a)–4(c), it is seen that the relative phase of the interferograms of v_B's=32 and 30 is almost the same between $\tau_{control}\simeq 1T_{vib}$ and $\tau_{control}\simeq(1+1/2)T_{vib}$, but it is shifted by π for v_B's=32 and 31 and for v_B's=32 and 33. The four different eigenstate interferograms are plotted together in Fig. 4(d) with their relative phases determined in Figs. 4(a)–4(c), as has already been done for $\tau_{control}\simeq 1\ T_{vib}$ in Fig. 3.

Furthermore, another two sets of the phase-jump measurements have been made by scanning $\tau_{control}$ around 630 fs $[\cong(1+1/4)T_{vib}]$ and 880 fs $[\cong(1+3/4)T_{vib}]$, and the results are shown in Figs. 5 and 6, respectively.

These results of phase-jump measurements can be easily explained by considering the $\tau_{control}$ dependence of the ρ_n given in Eq. (8). First we consider the eigenstate interfero-

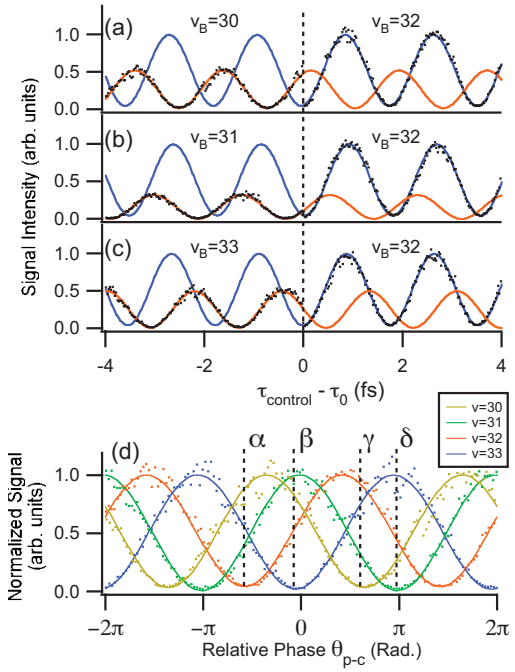

FIG. 6. (Color) Eigenstate interferogram measured with the pump-control delay $\tau_{control}$ tuned around $(1+3/4)\,T_{vib}$, where T_{vib} is a classical vibrational period of I_2. For the explanation of (a), (b), and (c), see the caption of Fig. 3. Black curves are measured data, and blue and red curves are the sine functions least square fitted to the regions on the right and left sides of the switching point, $\tau_{control}-\tau_0=0$, respectively. In the lowest panel, the four different eigenstate interferograms are plotted together with their relative phases determined in the upper three panels. See text for further details.

grams measured by scanning $\tau_{control}$ around $1\,T_{vib}$. From Eqs. (8) and (9), we can write

$$\rho_n(\tau_{control}) \propto [1+\cos(\omega_n\tau_{control})] = 1+\cos\left[\left(\omega_{\tilde{n}}+(n-\tilde{n})\frac{d\omega_n}{dn}+\frac{1}{2}(n-\tilde{n})^2\frac{d^2\omega_n}{dn^2}\right)\times(T_{vib}+\delta\tau_{control})\right], \quad (12)$$

where $\delta\tau_{control}$ is the small deviation of $\tau_{control}$ from $1T_{vib}$, that is, $\tau_{control}=1T_{vib}+\delta\tau_{control}$. Neglecting the second-order term, which represents the anharmonicity of the potential curve, and using Eq. (10), we have

$$\rho_n(\tau_{control}) \propto 1+\cos\left[\omega_{\tilde{n}}T_{vib}+\left(\omega_{\tilde{n}}+(n-\tilde{n})\frac{d\omega_n}{dn}\right)\delta\tau_{control}\right]. \quad (13)$$

Since $\omega_{\tilde{n}}$ is larger than $(n-\tilde{n})\frac{d\omega_n}{dn}$ by two orders of magnitude in the current system, Eq. (13) shows that the eigenstate interferograms $\rho_n(\tau_{control})$'s of the four levels $v_B=30-33$ oscillate nearly in phase with nearly the same frequency $\omega_{\tilde{n}}$ when $\delta\tau_{control}$ is scanned, i.e., when $\tau_{control}$ is scanned around $1T_{vib}$, if the anisotropy of the potential curve is neglected. This is consistent with the experimental results shown in Fig. 3(d). Because of this in-phase nature around $1T_{vib}$, it is possible to have the pump-control timings indicated in Fig. 3(d) by the lines α and β, where the populations of all the vibrational levels are almost at their maxima and minima, respectively. These timings α and β are expected to give time-domain pictures where a WP is once produced on the B state potential by the pump pulse, oscillates for one vibrational period, and then interacts with the second WP to give constructive and destructive interferences. In the next section, we demonstrate experimental observations of these real-time evolutions.

Next we consider the eigenstate interferograms measured by scanning $\tau_{control}$ around $(1+1/2)T_{vib}$. Using Eqs. (8) and (9) and neglecting the second-order term again, we can write

$$\rho_n(\tau_{control}) \propto 1+\cos\left[\frac{3}{2}\omega_{\tilde{n}}T_{vib}+\left(\omega_{\tilde{n}}+(n-\tilde{n})\frac{d\omega_n}{dn}\right)\times\delta\tau_{control}+(n-\tilde{n})\pi\right], \quad (14)$$

where, this time, $\delta\tau_{control}$ is the small deviation of $\tau_{control}$ from $(1+1/2)T_{vib}$, that is, $\tau_{control}=(1+1/2)T_{vib}+\delta\tau_{control}$. Equation (14) shows that the interferograms of the consecutive vibrational levels $v_B=n$ and $n+1$ are phase shifted by $\sim\pi$ if the potential anharmonicity is neglected. This means that the interferograms are almost in phase within each of the groups of even and odd n's, but are phase shifted by π between those two groups. This is consistent with the experimental results shown in Fig. 4(d). Among the four characteristic pump-control timings indicated in Fig. 4(d) by the lines α, β, γ, and δ, the timing α almost maximizes the populations of the odd levels and minimizes those of the even levels, and vice versa at the timing γ. The timings β and δ, on the other hand, give similar population distributions among the four levels. We demonstrate in the next section that these two similar distributions are actually accompanied with different relative phases among the four levels by comparing real-time evolutions of the WPs at these two timings β and δ.

Similar considerations for $\tau_{control}$ scanned around $(1+1/4)T_{vib}$ and $(1+3/4)T_{vib}$ show that the interferogram of $v_B=n+1$ is phase shifted from the one of $v_B=n$ by $\sim+\pi/2$ and $\sim-\pi/2$, respectively, if the potential anharmonicity is neglected. All four interferograms are, therefore, expected to be phase shifted from one another. This is consistent with the experimental results shown in Figs. 5(d) and 6(d). Because of the opposite sign of the relative phase between the consecutive levels, the relative orders of the four interferograms of $v_B=30-33$ in Figs. 5(d) and 6(d) are opposite; they are $33\rightarrow32\rightarrow31\rightarrow30$ in Fig. 5(d) and $30\rightarrow31\rightarrow32\rightarrow33$ in Fig. 6(d). By setting $\tau_{control}$ to the timing such as α, β, γ, or δ indicated in Figs. 5(d) and 6(d), we can selectively depopulate one of the four vibrational levels.

C. Coding at $\tau_{control}\simeq 1T_{vib}$

Figure 7 shows the population and phase codes taken with the pump and control timing $\tau_{control}$ tuned around $1T_{vib}$. Figures 7(a) and 7(b) show the population codes measured by

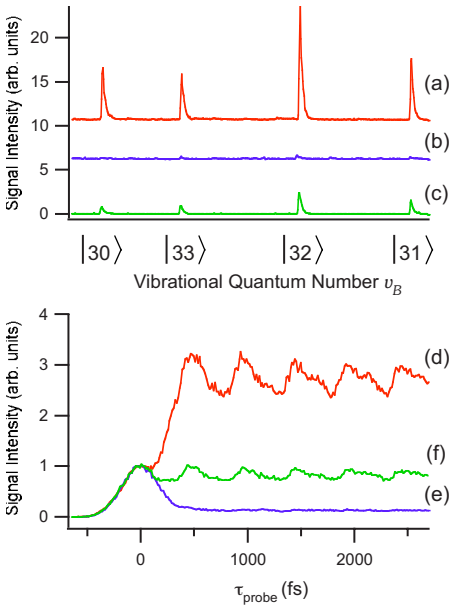

FIG. 7. (Color online) Wave-packet interference measured with the pump and control delay $\tau_{control}$ tuned to $\simeq 1\ T_{vib}$ ($\cong$500 fs), where T_{vib} is a classical vibrational period of I_2. (a), (b) $E-B$ excitation spectra, which we call the "population codes," measured by scanning the wavelength of the ns probe pulse. The relative phase θ_{p-c} of the pump and control pulses is different by $\sim\pi$ between (a) and (b). (c) Population code written without the control pulse and displayed for reference. The three population codes are displaced vertically from one another for clarity. See text for the normalization procedure. (d), (e) Real-time evolutions of the wave-packet interference, which we call the "phase codes," measured with almost the same θ_{p-c}'s as for (a) and (b), respectively. (f) Phase code written without the control pulse and displayed for reference. See text for the details of the data acquisition, the definition of $\tau_{probe}=0$, and the normalizing process. A possible deviation of θ_{p-c} within each set of the population and phase codes, (a)–(d) or (b)–(e), is estimated to be less than 0.03 π.

locking the relative phase of the pump and control pulses θ_{p-c} tuned around α and β, respectively, indicated in Fig. 3(d). Heights of the four peaks seen in each population code displayed in Fig. 7 represent the populations of the levels $v_B=30-33$ weighted by the FCFs of their relevant $E-B$ vibronic transitions. Each population code has been normalized by an average of the probe-pulse intensities monitored by a Si diode detector during its measurement. This normalization procedure is common to all of the population codes shown in the present paper.

Four peaks seen in each population code are assigned to $v_E=24\leftarrow v_B=30$, $26\leftarrow 33$, $25\leftarrow 32$, and $24\leftarrow 31$ vibronic transitions, based on their corresponding rotationless transition wavelengths 400.46, 400.75, 401.18, and 401.58 nm, respectively, calculated from the previous spectroscopic parameters [42,43]. The tail of each peak in its low-frequency side is due to the rotational substructures.

Figure 7(c) shows a reference code measured without the control pulse. As is seen from Fig. 3(d), code (a) is generated by the constructive interference of all the four eigenstates. Their peak heights are expected to be larger than those of the reference code (c) by a factor of $2^2=4$, since the constructive interference doubles an amplitude of each eigenstate, and its modulus square is measured in the population code. Similarly code (b) is generated by the destructive interference of all four eigenstates. These expected features agree well with the experimental observations shown in Figs. 7(a)–7(c).

Figures 7(d) and 7(e) show the phase codes taken with almost the same θ_{p-c}'s as for the population codes (a) and (b), respectively, and with the fs probe pulse tuned around 427.9 nm. Figure 7(f) shows a reference code measured without the control pulse. For the phase codes shown in Figs. 7(d)–7(f), each trace is a summation of four repeated scans. The origin of the probe delay ($\tau_{probe}=0$) denotes a position of the top of the first undulation in each measured trace. The position of the top was determined by smoothing the measured trace in units of seven data points. The vertical scaling of each trace is arbitrary and is normalized by the intensities around the top of its first undulation. These details of the data acquisition, the definition of $\tau_{probe}=0$, and the normalizing process are common to all of the phase codes shown in the present paper. The period of the beat structure is $\sim$500 fs. This agrees well with the period 498 fs calculated from the average energy spacing of the consecutive vibrational levels between $v_B=30$ and $v_B=33$ of the B state. It is seen from the phase codes in Figs. 7(d)–7(f) that the WP is once produced on the B state potential by the pump pulse, oscillates for one vibrational period, and then interacts with the second WP to give a drastic contrast between constructive and destructive interferences shown in Figs. 7(d) and 7(e), respectively. The ordinary frequency domain interpretation based on the spectral interference of twin pulses may be useful to elucidate population codes [20], but is no longer suitable for this real-time observation [21]. Similar correspondences between population distributions and beat structures have been recently predicted in theoretical simulations [22].

D. Coding at $\tau_{control}\simeq(1+\frac{1}{2})T_{vib}$

Figure 8 shows the population and phase codes taken with the pump and control timing $\tau_{control}$ tuned around $(1+1/2)T_{vib}$. Figures 8(a)–8(d) show the population codes measured by locking the relative phase of the pump and control pulses θ_{p-c} tuned around α, β, γ, and δ, respectively, indicated in Fig. 4(d). Figure 8(e) shows a reference code measured without the control pulse. It is seen from Figs. 8(a)–8(d) that the population code drastically changes as a function of θ_{p-c}, consistent with the eigenstate interferograms shown in Fig. 4(d).

Figures 8(f)–8(i) show the phase codes taken with almost the same θ_{p-c}'s as for the population codes 8(a)–8(d), respectively, and with the fs probe pulse tuned around 429.1 nm. Figure 8(j) shows a reference code measured without the control pulse. The phase code also has a clear dependence on θ_{p-c}. From these phase-code measurements made with the fs probe pulse, it is clearly seen that similar population codes 8(b) and 8(d) give distinct phase codes 8(g) and 8(i) in antiphase with each other, so that they can be clearly distinguished. Phase codes 8(f) and 8(h), on the other hand, correspond to population codes 8(a) and 8(c), each of which is

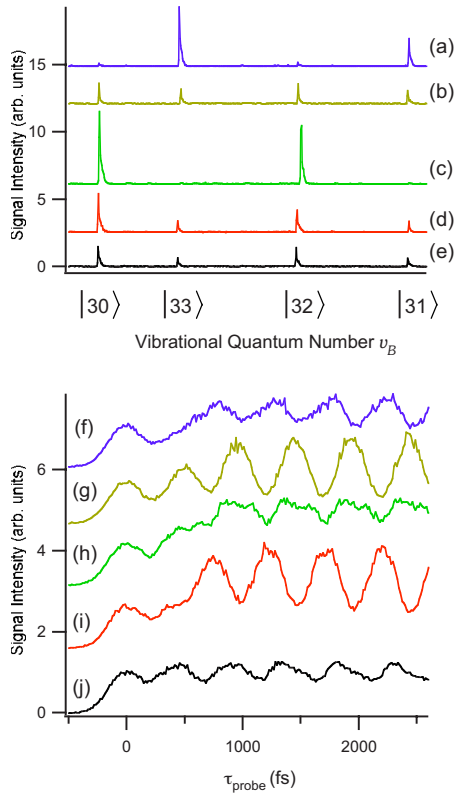

FIG. 8. (Color online) Wave packet interference measured with the pump and control delay $\tau_{control}$ tuned to $\simeq(1+1/2)T_{vib}$ ($\cong$760 fs), where T_{vib} is a classical vibrational period of I_2. (a)–(d) "Population codes" measured by scanning the wavelength of the ns probe pulse. The relative phase θ_{p-c} of the pump and control pulses is increased in steps of $\sim\pi/2$ in going from (a) to (d). (e) Population code written without the control pulse and displayed for reference. The five population codes are displaced vertically from one another for clarity. See text for the normalization procedure. (f)–(i) "Phase codes" measured with almost the same θ_{p-c}'s as for (a)–(d), respectively. (j) Phase code written without the control pulse and displayed for reference. The five phase codes are displaced vertically from one another for clarity. See text for the details of the data acquisition, the definition of $\tau_{probe}=0$, and the normalizing process. A possible deviation of θ_{p-c} within each set of the population and phase codes is estimated to be $<0.2\pi$ for the sets (a)–(f) and (c)–(h), and $<0.03\pi$ for (b)–(g) and (d)–(i).

composed of odd or even levels. Energy spacing of the odd or even levels involved in these codes is of course almost twice as large as that of the consecutive levels involved in codes 8(g) and 8(i). The beat period of codes 8(f) and 8(h) is, therefore, expected to be almost half of the period of codes 8(g) and 8(i). This is, however, not clearly seen in Figs. 8(f)–8(i); codes 8(f) and 8(h) still have a periodicity of about 500 fs, which is a characteristic period of codes 8(g) and 8(i). A similar counterintuitive feature has been observed also in our previous paper [21] for a different sets of v_B's prepared with a different pump and control wavelength around 610 nm. The reason for these counterintuitive observations is not clear at the moment, but one possible reason is that the structure of the beat is highly sensitive to the probe wavelength [37]; there may be a probe wavelength which gives a beat structure without the 500 fs periodicity. Further experimental and theoretical investigations are now in progress [44].

The WP created by a sequence of the pump and control pulses can be described as

$$\begin{aligned}|\psi(t)\rangle &= \sum_{n=30}^{33} a_n|n\rangle e^{-i\omega_n t} + \sum_{n=30}^{33} a_n|n\rangle e^{-i\omega_n(t-\tau_{control})} \\ &= |30\rangle e^{-i\omega_{30}t}(1+e^{i\omega_{32}\tau_{control}}e^{i(\omega_{30}-\omega_{32})\tau_{control}}) \\ &+ |31\rangle e^{-i\omega_{31}t}(1+e^{i\omega_{32}\tau_{control}}e^{i(\omega_{31}-\omega_{32})\tau_{control}}) \\ &+ |32\rangle e^{-i\omega_{32}t}(1+e^{i\omega_{32}\tau_{control}}) \\ &+ |33\rangle e^{-i\omega_{33}t}(1+e^{i\omega_{32}\tau_{control}}e^{i(\omega_{33}-\omega_{32})\tau_{control}}), \quad (15)\end{aligned}$$

with $a_n=1$ for all vibrational levels for simplicity. Since $\tau_{control}$ is tuned around $(1+1/2)T_{vib}$,

$$\tau_{control} \simeq \left(1+\tfrac{1}{2}\right)T_{vib} = \frac{3\pi}{\left.\frac{d\omega_n}{dn}\right|_{n=32}}, \quad (16)$$

where T_{vib} is substituted by Eq. (10). Replacing $\tau_{control}$'s in Eq. (15) by Eq. (16) and considering $\omega_{30}-\omega_{32}\simeq-2\left.\frac{d\omega_n}{dn}\right|_{n=32}$, $\omega_{31}-\omega_{32}\simeq-\left.\frac{d\omega_n}{dn}\right|_{n=32}$, and $\omega_{33}-\omega_{32}\simeq\left.\frac{d\omega_n}{dn}\right|_{n=32}$, we have

$$\begin{aligned}|\psi(t)\rangle &\simeq |30\rangle e^{-i\omega_{30}t}(1+e^{i\omega_{32}\tau_{control}}e^{-6\pi i}) \\ &+ |31\rangle e^{-i\omega_{31}t}(1+e^{i\omega_{32}\tau_{control}}e^{-3\pi i}) \\ &+ |32\rangle e^{-i\omega_{32}t}(1+e^{i\omega_{32}\tau_{control}}) \\ &+ |33\rangle e^{-i\omega_{33}t}(1+e^{i\omega_{32}\tau_{control}}e^{3\pi i}). \quad (17)\end{aligned}$$

From Eq. (17), the pump-control phases $\alpha-\delta$ indicated in Fig. 4(d) almost correspond to $\omega_{32}\tau_{control}=(2k-1)\pi$, $(2k-1/2)\pi$, $2k\pi$, and $(2k+1/2)\pi$, respectively, with k being an integer. The WPs created with θ_{p-c}'s tuned to $\alpha-\delta$ indicated in Fig. 4(d) can be described, respectively, as

$$\begin{aligned}|\psi_\alpha(t)\rangle &\simeq 0|30\rangle e^{-i\omega_{30}t} + 2|31\rangle e^{-i\omega_{31}t} \\ &+ 0|32\rangle e^{-i\omega_{32}t} + 2|33\rangle e^{-i\omega_{33}t}, \\ |\psi_\beta(t)\rangle &\simeq (1-i)|30\rangle e^{-i\omega_{30}t} + (1+i)|31\rangle e^{-i\omega_{31}t} \\ &+ (1-i)|32\rangle e^{-i\omega_{32}t} + (1+i)|33\rangle e^{-i\omega_{33}t}, \\ |\psi_\gamma(t)\rangle &\simeq 2|30\rangle e^{-i\omega_{30}t} + 0|31\rangle e^{-i\omega_{31}t} + 2|32\rangle e^{-i\omega_{32}t} \\ &+ 0|33\rangle e^{-i\omega_{33}t}, \\ |\psi_\delta(t)\rangle &\simeq (1+i)|30\rangle e^{-i\omega_{30}t} + (1-i)|31\rangle e^{-i\omega_{31}t} \\ &+ (1+i)|32\rangle e^{-i\omega_{32}t} + (1-i)|33\rangle e^{-i\omega_{33}t}. \quad (18)\end{aligned}$$

From these equations, it is seen that the even levels are phase shifted from the odd levels by $\sim-\pi/2$ at β and by $\sim+\pi/2$ at δ. Therefore the relative phase of the even and odd levels is shifted by π between β and δ. This phase information is of course unable to be retrieved in the population measurements in the frequency domain, where the modulus square of the amplitude of each eigenfunction is measured. The present antiphase beats in Figs. 8(g) and 8(i)

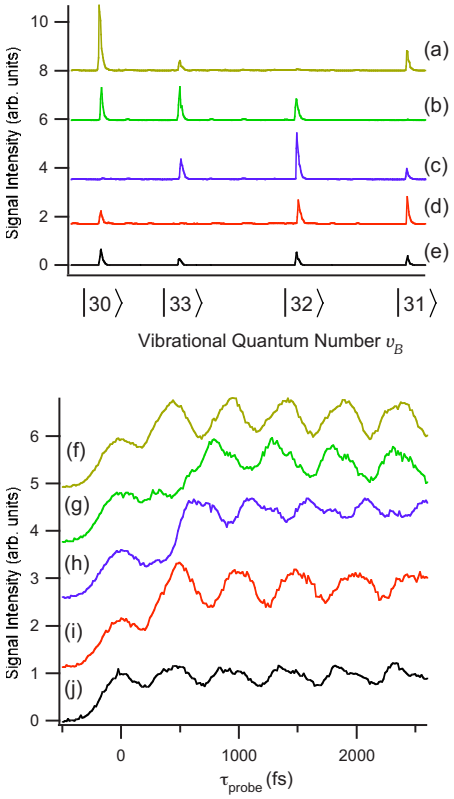

FIG. 9. (Color online) Wave-packet interference measured with the pump and control delay $\tau_{control}$ tuned to $\simeq(1+1/4)T_{vib}$ ($\cong$630 fs). (a)–(d) "Population codes" measured by scanning the wavelength of the ns probe pulse. The relative phase θ_{p-c} of the pump and control pulses is increased in steps of $\sim\pi/2$ in going from (a) to (d). (e) Population code written without the control pulse and displayed for reference. The five population codes are displaced vertically from one another for clarity. See text for the normalization procedure. (f)–(i) "Phase codes" measured with almost the same θ_{p-c}'s as for (a)–(d), respectively. (j) Phase code written without the control pulse and displayed for reference. The five phase codes are displaced vertically from one another for clarity. See text for the details of the data acquisition, the definition of $\tau_{probe}=0$, and the normalizing process. A possible deviation of θ_{p-c} within each set of the population and phase codes, (a)–(f), (b)–(g), (c)–(h), or (d)–(i), is estimated to be less than 0.03π.

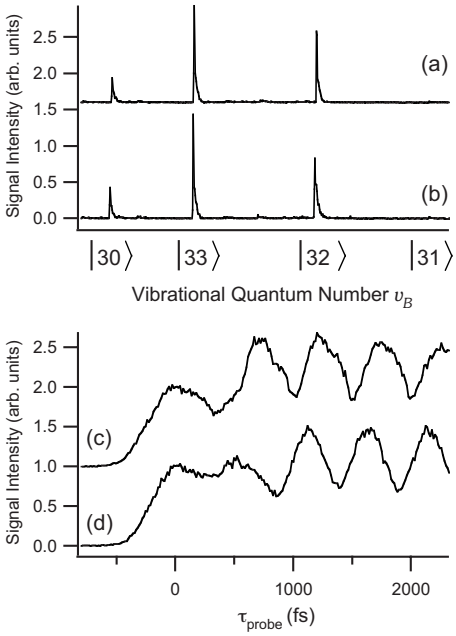

FIG. 10. Wave-packet interference measured with the pump and control delay $\tau_{control}$ tuned to $\simeq(1+1/4)T_{vib}$ ($\cong$630 fs) and $\simeq(1+3/4)T_{vib}$ ($\cong$880 fs), where T_{vib} is a classical vibrational period of I_2. (a), (b) "Population codes" measured by scanning the wavelength of the ns probe pulse. The delay $\tau_{control}$ is tuned to (a) $\simeq(1+1/4)T_{vib}$ and (b) $\simeq(1+3/4)T_{vib}$. The relative phase θ_{p-c} of the pump and control pulses is tuned to depopulate the level $v_B=31$ in both (a) and (b). The two population codes are displaced vertically from one another for clarity. See text for the normalization procedure. (c), (d) "Phase codes" measured with almost the same θ_{p-c}'s as for (a) and (b), respectively. The two phase codes are displaced vertically from one another for clarity. See text for the details of the data acquisition, the definition of $\tau_{probe}=0$, and the normalizing process. A possible deviation of θ_{p-c} within each set of the population and phase codes, (a)–(c) or (b)–(d), is estimated to be less than 0.03 π.

are thus attributable to this π shift in the relative phase of the odd and even levels between β and δ; these two θ_{p-c}'s, however, give similar codes to be barely distinguishable in the population measurements. A combination of the population code and the phase code thus retrieves both the amplitude and phase information written in WPs [21].

E. Coding at $\tau_{control}\simeq(1+\frac{1}{4})T_{vib}$ and $\simeq(1+\frac{3}{4})T_{vib}$

Another set of measurements of the population and phase codes has been made with $\tau_{control}$ tuned around $(1+1/4)T_{vib}$. Figures 9(a)–9(d) show four different population codes taken with four different θ_{p-c}'s spaced in steps of $\sim\pi/2$. Figure 9(e) shows a reference code measured without the control pulse. Again the population code drastically changes as a function of θ_{p-c}, consistent with the eigenstate interferograms shown in Fig. 5(d). It is seen in Figs. 9(a)–9(d) that one of the four vibrational levels is selectively depopulated.

Figures 9(f)–9(i) show the phase codes taken with almost the same θ_{p-c}'s as for the population codes 9(a)–9(d), respectively, and with the fs probe pulse tuned around 430.5 nm. Figure 9(j) shows a reference code measured without the control pulse. The phase code also has a clear dependence on θ_{p-c} again.

It is expected from the eigenstate interferograms shown in Figs. 5(d) and 6(d) that similar population codes can be prepared with different $\tau_{control}$'s tuned around $(1+1/4)T_{vib}$ and $(1+3/4)T_{vib}$. Figures 10(a) and 10(b) show two population codes measured with two different $\tau_{control}$'s tuned around $(1+1/4)T_{vib}$ and $(1+3/4)T_{vib}$, respectively. The fine tuning of $\tau_{control}$'s was chosen so that the population of $v_B=31$ could be the minimum. These two population codes are very similar, difficult to be distinguished from each other. Figures 10(c) and 10(d) show the phase codes taken with almost the same θ_{p-c}'s as for the population codes 10(a) and 10(b), respectively, and with the fs probe pulse tuned around 426.9 nm.

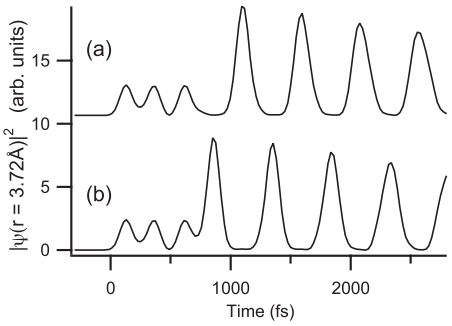

FIG. 11. Real-time evolution of the wave-packet interference simulated with the pump and control delay τ_{control} tuned to $\simeq(1+1/2)T_{\text{vib}}$, where T_{vib} is a classical vibrational period of I_2; (a) $\tau_{\text{control}}=734.45$ fs and (b) $\tau_{\text{control}}=735.35$ fs. The abscissa is the time measured from the center of the pump pulse. The modulus square of the wave-packet amplitude at the internuclear distance of 3.72 Å is plotted as a function of time. The pump and control phases $\theta_{\text{p-c}}$'s in (a) and (b) almost correspond to those of the observed beats shown in Figs. 8(g) and 8(i), respectively.

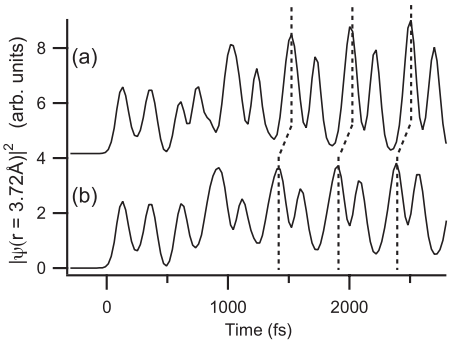

FIG. 12. Real-time evolution of the wave-packet interference simulated with the pump and control delay τ_{control} tuned to $\simeq(1+1/4)T_{\text{vib}}$ and $\simeq(1+3/4)T_{\text{vib}}$, where T_{vib} is a classical vibrational period of I_2; (a) $\tau_{\text{control}}=614.40$ fs and (b) $\tau_{\text{control}}=858.00$ fs. The abscissa is the time measured from the center of the pump pulse. The modulus square of the wave-packet amplitude at the internuclear distance of 3.72 Å is plotted as a function of time. The pump and control phases $\theta_{\text{p-c}}$'s in (a) and (b) almost correspond to those of the observed beats shown in Figs. 10(c) and 10(d), respectively.

From these phase-code measurements made with the fs probe pulse, it is seen that similar population codes 10(a) and 10(b) give distinct phase codes 10(c) and 10(d), where the beat structures are phase shifted from each other, so that they can be distinguished. Instead of the clear π phase shift seen in Figs. 8(g) and 8(i), code 10(d) is phase shifted from code 10(c) by $\sim\pi/2$ in the current case. The WPs are described as

$$|\psi_c(t)\rangle \simeq (1+i)|30\rangle e^{-i\omega_{30}t} + 0|31\rangle e^{-i\omega_{31}t} + (1-i)|32\rangle e^{-i\omega_{32}t} + 2|33\rangle e^{-i\omega_{33}t}, \quad (19)$$

$$|\psi_d(t)\rangle \simeq (1-i)|30\rangle e^{-i\omega_{30}t} + 0|31\rangle e^{-i\omega_{31}t} + (1+i)|32\rangle e^{-i\omega_{32}t} + 2|33\rangle e^{-i\omega_{33}t}, \quad (20)$$

for codes 10(c) and 10(d), respectively. The present $\pi/2$ phase shift of the beat structures is thus attributable to the $\pi/2$ phase shift in the wave functions of the levels $v_B=30$ and 32 relative to the level $v_B=33$ between codes 10(c) and 10(d).

V. SIMULATION

In this section we show the results of theoretical simulations of the temporal evolutions of WPs created by the phase-locked pump and control pulses. Time dependent Schrödinger equation was solved by using the split operator algorithm [45,46]. For simplicity, Morse potentials were used for calculations of the eigenvalues and eigenfunctions of the X and B states [47]. Since we are interested in the WP motion on the B state potential curve, we did not include the interaction with the probe pulse. The pump and control pulses were assumed to be Gaussian pulses centered at 532 nm, and their pulse width was taken to be 70 fs in FWHM. The initial rovibrational state of the molecule was taken to be $v_X=0$, and $J_X=0$. The contributions from higher rotational levels were not included for simplicity.

Figure 11 shows simulated temporal evolutions of WPs on the B-state potential obtained with τ_{control} tuned around $(1+1/2)$ T_{vib}. The abscissa is the time measured from the center of the pump pulse. The modulus square of the wave-packet amplitude at 3.72 Å in the internuclear distance, which corresponds to 429.2 nm in the probe wavelength under the classical Franck-Condon approximation [37], is plotted as a function of time. The delay τ_{control} was tuned to 734.45 fs and 735.35 fs in Figs. 11(a) and 11(b), respectively. These values were determined from the simulated eigenstate interferograms so that the pump and control phases $\theta_{\text{p-c}}$'s in Figs. 11(a) and 11(b) almost corresponded to the $\theta_{\text{p-c}}$'s indicated by the lines β and δ in Fig. 4(d). The difference of these τ_{control}'s from the experimental values used in the previous chapters is ascribed to the difference between the real potential and the Morse potential used in the present theoretical simulations. The π phase flip seen in the observed beat structures shown in Figs. 8(g) and 8(i) is well reproduced in the simulations shown in Figs. 11(a) and 11(b).

Figure 12 shows similar simulated results obtained with τ_{control} tuned around $(1+1/4)$ T_{vib} and $(1+3/4)$ T_{vib}; (a) $\tau_{\text{control}}=614.40$ fs $[\cong(1+1/4)T_{\text{vib}}]$ and (b) $\tau_{\text{control}}=858.00$ fs $[\cong(1+3/4)T_{\text{vib}}]$. The pump and control phases $\theta_{\text{p-c}}$'s in Figs. 12(a) and 12(b) almost correspond to those of the observed beats shown in Figs. 10(c) and 10(d). The observed $\pi/2$ phase shift of the beats is reproduced in the simulations.

VI. COMPARISON WITH OTHER APPROACHES

The retrieval of amplitude and phase information of WPs has so far been demonstrated by several groups with different techniques. Weinacht *et al.* reconstructed the electronic WP composed of Rydberg wave functions in the Cs atom by measuring a population distribution created by interference with another reference WP [8]. A similar effort to characterize both momentum and position information of a WP has

been made for a vibrational WP in the Na dimer by measuring the time- and frequency-resolved spectrum of spontaneous emission [48,49]. Recently, Monmayrant *et al.* reported another holographic method to rebuild the spin-orbit WP of the Rb atom [50]. They applied a phase-locked pair of fs pulses to prepare the WPs, where the first pulse was an Fourier-transform limited pulse, and the second one was a chirped pulse. From the coherent transient structure due to the superposition of the WPs created by the first and the second pulses, they could calculate the real and imaginary parts of the spin-orbit WP.

Our present approach with a combination of the population code and the phase code is another possibility to retrieve the full quantum information of WPs. It is a straightforward and robust approach, and is applicable to wide range of quantum systems.

Aside from these linear interferometry, nonlinear WPI with two phase-locked pairs of optical pulses has been demonstrated theoretically by Humble *et al.* [51,52] to reconstruct the rovibrational WP of the Li dimer.

VII. CONCLUSION

In summary, we have employed high-precision molecular WP interferometry to read and write amplitude and phase information in a set of vibrational eigenstates of the iodine molecule. Quantum interference of two vibrational WPs in the iodine molecule has been controlled by using a pair of phase-locked fs laser pulses, and a population distribution of the vibrational eigenstates produced by that interference has been measured with a narrow-band ns probe laser pulse. The population distribution, which we call a population code, is highly sensitive to a combination of the relative delay τ_{control} and the relative phase $\theta_{\mathrm{p-c}}$ between the locked pulses stabilized on the attosecond time scale. We have also measured a real-time evolution of the WP interference with another fs probe laser pulse. The real-time evolution, which we call a phase code, is also highly sensitive to τ_{control} and $\theta_{\mathrm{p-c}}$, giving information on the relative phases among the vibrational eigenstates within a WP. The ordinary frequency domain interpretation based on the spectral interference of the locked pulses may be useful to elucidate τ_{control} and $\theta_{\mathrm{p-c}}$ dependence of the population code, but is no longer suitable for the present dependence of the phase codes on τ_{control} and $\theta_{\mathrm{p-c}}$. Moreover, the phase code has allowed us to obtain additional phase information unable to be obtained from the population codes. The combination of the population code and the phase code is useful to obtain both amplitude and phase information written and stored in a WP. Reading and writing amplitude and phase information of wave functions are indispensable for developing novel quantum technologies such as atom- and molecule-based information processing [8,21,53]. We have also performed numerical simulations of the phase code, and the characteristic features of its τ_{control} and $\theta_{\mathrm{p-c}}$ dependences have been well reproduced. Development of quantum gates is now in progress as a next step to the present reading and writing, based on our high-precision molecular WP interferometry.

ACKNOWLEDGMENTS

The authors gratefully acknowledge Dr. J.- Ch. Delagnes (IMS) for his contribution to the preparation of the optical pulse stretcher for the bandwidth reduction system. The authors are also grateful to Dr. J.-Ch. Delagnes and Dr. M. Fushitani (IMS) for their critical readings of this manuscript. This work was partly supported by Grant in Aid from MEXT of Japan (Grant No. 15204034, No. 17740269, and No. 18340121) and Priority Area: "Control of Molecules in Intense Laser Fields."

[1] N. F. Scherer, R. J. Carlson, A. Matro, M. Du, A. J. Ruggiero, V. Romero-Rochin, J. A. Cina, G. R. Fleming, and S. A. Rice, J. Chem. Phys. **95**, 1487 (1991).
[2] N. F. Scherer, A. Matro, L. D. Ziegler, M. Du, R. J. Carlson, J. A. Cina, and G. R. Fleming, J. Chem. Phys. **96**, 4180 (1992).
[3] M. W. Noel and C. R. Stroud, Jr., Phys. Rev. Lett. **75**, 1252 (1995); **77**, 1913 (1996); Opt. Express **1**, 176 (1997).
[4] R. R. Jones, C. S. Raman, D. W. Schumacher, and P. H. Bucksbaum, Phys. Rev. Lett. **71**, 2575 (1993).
[5] R. R. Jones, D. W. Schumacher, T. F. Gallagher, and P. H. Bucksbaum, J. Phys. B **28**, L405 (1995).
[6] R. R. Jones, Phys. Rev. Lett. **75**, 1491 (1995).
[7] D. W. Schumacher, J. H. Hoogenraad, D. Pinkos, and P. H. Bucksbaum, Phys. Rev. A **52**, 4719 (1995).
[8] T. C. Weinacht, J. Ahn, and P. H. Bucksbaum, Phys. Rev. Lett. **80**, 5508 (1998); J. Ahn, T. C. Weinacht, and P. H. Bucksbaum, Science **287**, 463 (2000).
[9] L. D. Noordam, D. I. Duncan, and T. F. Gallagher, Phys. Rev. A **45**, 4734 (1992).
[10] B. Broers, J. F. Christian, J. H. Hoogenraad, W. J. van der Zande, H. B. van Linden van den Heuvell, and L. D. Noordam, Phys. Rev. Lett. **71**, 344 (1993).
[11] J. F. Christian, B. Broers, J. H. Hoogenraad, W. J. van der Zande, and L. D. Noordam, Opt. Commun. **103**, 79 (1993).
[12] J. F. Christian and B. Broers, Phys. Rev. A **52**, 3655 (1995).
[13] L. Marmet, H. Held, G. Raithel, J. A. Yeazell, and H. Walther, Phys. Rev. Lett. **72**, 3779 (1994).
[14] V. Blanchet, C. Nicole, M. A. Bouchene, and B. Girard, Phys. Rev. Lett. **78**, 2716 (1997).
[15] M. A. Bouchene, V. Blanchet, C. Nicole, N. Melikechi, B. Girard, H. Ruppe, S. Rutz, E. Schreiber, and L. Wöste, Eur. Phys. J. D **2**, 131 (1998).
[16] M. Bellini, A. Bartoli, and T. W. Hänsch, Opt. Lett. **22**, 540 (1997).
[17] V. Blanchet, M. A. Bouchene, and B. Girard, J. Chem. Phys. **108**, 4862 (1998).
[18] V. Blanchet, M. A. Bouchene, O. Cabrol, and B. Girard, Chem. Phys. Lett. **233**, 491 (1995).
[19] Ch. Warmuth, A. Tortschanoff, F. Milota, M. Shapiro, Y. Prior, I. Sh. Averbukh, W. Schleich, W. Jakubetz, and H. F. Kauffmann, J. Chem. Phys. **112**, 5060 (2000); **114**, 9901 (2001).
[20] K. Ohmori, Y. Sato, E. E. Nikitin, and S. A. Rice, Phys. Rev.

Lett. **91**, 243003 (2003).
[21] K. Ohmori, H. Katsuki, H. Chiba, M. Honda, Y. Hagihara, K. Fujiwara, Y. Sato, and K. Ueda, Phys. Rev. Lett. **96**, 093002 (2006).
[22] E. D. Boleat and H. H. Fielding, Mol. Phys. **103**, 491 (2005).
[23] E. W. Lerch, X. Dai, S. Gilb, E. A. Torres, and S. R. Leone, J. Chem. Phys. **124**, 044306 (2006).
[24] C. Petersen, E. Péronne, J. Thøgersen, H. Stapelfeldt, and M. Machholm, Phys. Rev. A **70**, 033404 (2004).
[25] E. Skovsen, M. Machholm, T. Ejdrup, J. Thøgersen, and H. Stapelfeldt, Phys. Rev. Lett. **89**, 133004 (2002).
[26] M. Wollenhaupt, A. Assion, D. Liese, Ch. Sarpe-Tudoran, T. Baumert, S. Zamith, M. A. Bouchene, B. Girard, A. Flettner, U. Weichmann, and G. Gerber, Phys. Rev. Lett. **89**, 173001 (2002).
[27] T. Brixner, G. Krampert, T. Pfeifer, R. Selle, G. Gerber, M. Wollenhaupt, O. Graefe, C. Horn, D. Liese, and T. Baumert, Phys. Rev. Lett. **92**, 208301 (2004).
[28] A. Präkelt, M. Wollenhaupt, C. Sarpe-Tudoran, and T. Baumert, Phys. Rev. A **70**, 063407 (2004).
[29] A. P. Heberle, J. J. Baumberg, and K. Köhler, Phys. Rev. Lett. **75**, 2598 (1995).
[30] M. Fushitani, M. Bargheer, M. Gühr, and N. Schwentner, Phys. Chem. Chem. Phys. **7**, 3143 (2005).
[31] M. Gruebele and A. H. Zewail, J. Chem. Phys. **98**, 883 (1993).
[32] M. Gruebele, G. Roberts, M. Dantus, R. M. Bowman, and A. H. Zewail, Chem. Phys. Lett. **166**, 459 (1990).
[33] J. A. Paisner and R. Wallenstein, J. Chem. Phys. **61**, 4317 (1974).
[34] M. Broyer, J. Vigué, and J. C. Lehmann, J. Chem. Phys. **63**, 5428 (1975).
[35] J. Tellinghuisen, J. Quant. Spectrosc. Radiat. Transf. **19**, 149 (1978).
[36] I. S. Averbukh and N. F. Perelman, Phys. Lett. A **139**, 449 (1989).
[37] H. Katsuki, H. Chiba, B. Girard, C. Meier, and K. Ohmori, Science **311**, 1589 (2006).
[38] T. Lohmüller, V. Engel, J. A. Beswick, and C. Meier, J. Chem. Phys. **120**, 10442 (2004).
[39] J. A. Yeazell, M. Mallalieu, and C. R. Stroud, Jr., Phys. Rev. Lett. **64**, 2007 (1990).
[40] J. A. Yeazell and C. R. Stroud, Jr., Phys. Rev. A **43**, 5153 (1991).
[41] M. Nauenberg, J. Phys. B **23**, L385 (1990).
[42] P. Luc, J. Mol. Spectrosc. **80**, 41 (1980).
[43] J. C. D. Brand, A. R. Hoy, A. K. Kalkar, and A. B. Yamashita, J. Mol. Spectrosc. **95**, 350 (1982).
[44] H. Katsuki, H. Chiba, B. Girard, C. Meier, and K. Ohmori (unpublished).
[45] M. D. Feit, J. A. Fleck, Jr., and A. Steiger, J. Comput. Phys. **47**, 412 (1982).
[46] R. Kosloff, J. Phys. Chem. **92**, 2087 (1988).
[47] V. V. Yakovlev, C. J. Bardeen, J. Che, J. Cao, and K. R. Wilson, J. Chem. Phys. **108**, 2309 (1998).
[48] T. J. Dunn, I. A. Walmsley, and S. Mukamel, Phys. Rev. Lett. **74**, 884 (1995).
[49] T. J. Dunn, J. N. Sweetser, I. A. Walmsley, and C. Radzewicz, Phys. Rev. Lett. **70**, 3388 (1993).
[50] A. Monmayrant, B. Chatel, and B. Girard, Phys. Rev. Lett. **96**, 103002 (2006); Opt. Commun. **264**, 256 (2006).
[51] T. S. Humble and J. A. Cina, J. Phys. Chem. B **110**, 18879 (2006).
[52] T. S. Humble and J. A. Cina, Phys. Rev. Lett. **93**, 060402 (2004).
[53] Z. Amitay, R. Kosloff, and S. R. Leone, Chem. Phys. Lett. **359**, 8 (2002).